Early arrival waveform inversion of shallow seismic land data

Sherif M. Hanafy and Han Yu, King Abdullah University of Science and Technology (KAUST)*

Summary

We estimate the near-surface velocity distribution over Wadi Qudaid in Saudi Arabia by applying early arrival waveform inversion (EWI) to shallow seismic land data collected with source-receiver offsets no longer than 232 m. The main purpose is to characterize the shallow subsurface for its water storage and reuse potential. To enhance the accuracy of EWI, we extracted a natural source wavelet from the data, and also corrected for the attenuation effects with an estimated factor Q. Results suggest that, compared to traveltime tomography, EWI can generate a highly resolved velocity tomogram from shallow seismic data. The more accurate EWI tomogram can make an economically important difference in assessing the storage potential of this wadi; in this case we find an increase of 18% of storage potential in the EWI tomogram relative to the traveltime tomogram. This approach suggests that FWI might be a more accurate means for economically characterizing the water storage potential for wadis' throughout the world.

Introduction

Full waveform inversion (FWI) (Tarantola, 1984) is an effective method for reconstructing highly resolved models of the earth's velocity distribution. It can be implemented in either the space-frequency (Pratt et al., 1998) or the space-time domains (Zhou et al., 1995). However, FWI is computationally expensive and its misfit function is highly nonlinear with respect to velocity perturbations. To partly mitigate these problems, Sheng et al. (2006) proposed an early arrival waveform inversion (EWI) method for near-surface refraction data. This approach with the acoustic wave equation can accurately invert land data if the early arrivals are mostly free of elastic effects (Buddenseik, 2004). In this work, our goal is to characterize the shallow subsurface for its water storage and reuse by applying the approach of Sheng et al. (2006) to seismic early arrival data collected at Wadi Qudaid, 100 km north of Jeddah, Saudi Arabia. Compared to traveltime tomography, we believe that the more accurate EWI tomogram will make an economically important difference in characterizing the water storage potential in this wadi.

Since the subsurface soils are partially saturated, the attenuation factor Q is required to correct for attenuation effects in the data prior to inversion. Compared to FWI, early arrival waveform inversion (EWI) also avoids a high-frequency assumption but has more reliable convergence properties because it needs to explain only the early arrivals in the recorded traces.

Theory

The early arrival waveform inversion of Sheng et al. (2006) assumes the acoustic wave equation,

$$\frac{1}{c^2(\boldsymbol{x})}\frac{\partial^2 p(\boldsymbol{x},t|\boldsymbol{x}_s)}{\partial t^2} - \nabla^2 p(\boldsymbol{x},t|\boldsymbol{x}_s) = s(\boldsymbol{x},t|\boldsymbol{x}_s), \qquad (1)$$

where $p(\boldsymbol{x},t|\boldsymbol{x}_s)$ denotes the pressure field at position $\boldsymbol{x}$, time t, and a source at $\boldsymbol{x}_s$. The velocity model is represented by $c(\boldsymbol{x})$, and $s(\boldsymbol{x},t|\boldsymbol{x}_s)$ is the source function. The solution to equation 1 can be calculated by a finite-difference method (Levander, 1988). The solution can also be written in terms of its Green's function $g(\boldsymbol{x},t|\boldsymbol{x}',0)$ associated with a source at $\boldsymbol{x}'$ as

$$p(\boldsymbol{x},t|\boldsymbol{x}_s) = \int g(\boldsymbol{x},t|\boldsymbol{x}',0) * s(\boldsymbol{x}',t|\boldsymbol{x}_s)d\boldsymbol{x}', \qquad (2)$$

where the symbol * denotes temporal convolution. We ignore the shear wave effects in the wave equation (Zhou et al., 1995), because the early arrivals in the 2D near-surface seismic data contain few elastic effects.

FWI estimates the velocity model by minimizing the early arrival misfit function (Boonyasiriwat et al., 2010), where the waveform data residual is defined as

$$\Delta p(\boldsymbol{x}_g,t|\boldsymbol{x}_s) = \left[p_{obs}(\boldsymbol{x}_g,t|\boldsymbol{x}_s) - p_{calc}(\boldsymbol{x}_g,t|\boldsymbol{x}_s)\right]W(\boldsymbol{x}_g,t|\boldsymbol{x}_s), \qquad (3)$$

Here, $\boldsymbol{x}_g$ is the receiver position vector, p_{obs} and p_{calc} are, respectively, the observed and calculated data, and $W(\boldsymbol{x}_g,t|\boldsymbol{x}_s)$ is a window function that mutes all the energy except for the early arrivals. The velocity model $c(\boldsymbol{x})$ is iteratively updated by minimizing the misfit functional E, represented by the L_2 norm of the data residuals over time and space,

$$E = \frac{1}{2}\sum_s\sum_g\int(\Delta p(\boldsymbol{x}_g,t|\boldsymbol{x}_s))^2\,dt, \qquad (4)$$

A nonlinear conjugate-gradient method (Luo and Schuster, 1991) is used to minimize the gradient function. The gradient of the misfit functional E with respect to changes in the velocity $c(\boldsymbol{x})$ is the first variation (Logan, 1996) of E at the vector point $c(\boldsymbol{x})$ in the direction of $\delta c(\boldsymbol{x})$. This gradient $\left[grad(\boldsymbol{x}) = \frac{\partial E}{\partial \delta c(\boldsymbol{x})}\right]$ is computed by migrating the waveform residuals in time (Tarantola, 1984),

DOI http://dx.doi.org/10.1190/segam2013-0351.1

$$grad(\boldsymbol{x}) = \frac{1}{c^3(\boldsymbol{x})} \sum_s \int \dot{p}_f(\boldsymbol{x}, t|\boldsymbol{x}_s) \dot{p}_b(\boldsymbol{x}, t|\boldsymbol{x}_s)\, dt, \qquad (5)$$

where $\dot{p}$ is the time derivative of p, $p_f(x, t|x_s)$ and $p_b(x, t|x_s)$ represent the forward-propagated and back-projected wavefields, respectively.

The velocity model can be iteratively updated along the conjugate directions defined by

$$\boldsymbol{d}_k = -\boldsymbol{P}_k \boldsymbol{g}_k + \beta_k \boldsymbol{d}_{k-1}, \qquad (6)$$

where $k = 1,2, \ldots, k_{max}$, $g=[grad(\boldsymbol{x})]$, and $\boldsymbol{P}$ is the conventional geometrical-spreading preconditioner (Causse et al., 1999). The parameter β_k is calculated by the Polak-Ribiere formula (Norcedal and Wright, 1999)

$$\beta_k = \frac{\boldsymbol{g}_k^T(\boldsymbol{P}_k - \boldsymbol{P}_{k-1}\boldsymbol{g}_{k-1})}{\boldsymbol{g}_{k-1}^T \boldsymbol{P}_{k-1} \boldsymbol{g}_{k-1}}, \qquad (7)$$

and the velocity model is updated by

$$c_{k+1}(\boldsymbol{x}) = c_k(\boldsymbol{x}) + \lambda_k \boldsymbol{d}_k(\boldsymbol{x}), \qquad (8)$$

where λ_k is the step length which can be determined by a quadratic line-search method (Nocedal and Wright, 1999), and $d_k(\boldsymbol{x})$ is the component of the direction vector $d_k(\boldsymbol{x})$ indexed by $\boldsymbol{x}$. The initial velocity model $c_0(x)$ is the traveltime tomogram, and equation 8 is iteratively applied until the misfit functional E satisfies a stopping criterion.

Numerical Test: 2D Near-Surface Refraction Survey, Wadi Qudaid

The 2D seismic survey is conducted at Wadi Qudaid (Figure 1a and 1b) around 100 km north of Jeddah, KSA. It consists of one line of 117 vertical component geophones with 2.0 m spacing and one shot at every receiver position. A 200 lb weight drop (Figure 1c) was used to generate the seismic energy with 15 stacks at each shot location. For this data set, the dominant wavelength and the dominant frequency of the first arrival head waves are estimated to be 6 m and 60 Hz, respectively, where the minimum P-wave velocity is estimated to be 350 m/s.

The land data are first processed to reduce elastic effects in the field data. In this work we followed a 4-step processing scheme;

1. Trace normalization
2. Attenuation compensation
3. Corrections for 3D geometrical spreading
4. Bandpass filtering (15 – 70 Hz)

According to Liao and McMechan (1997), the linear attenuation transfer function $T(f) = e^{-f\pi t/Q}$, which transfers the input spectrum *S(f)* to the output *R(f)* at frequency *f* by *R(f)* = *T(f) S(f)*. The attenuation factor *Q* can be obtained by $f_r = f_s - \frac{2\pi\sigma_s^2}{Q}t$, where f_r and f_s are respectively centroid frequencies of the first arrival at the receiver and the source, and σ_s^2 is the variance of the source spectrum. Figure 2 shows the centroid frequencies f_r plotted against traveltimes *t* of the first arrivals. The variance σ_s^2 of the source spectrum is equal to 312.7 Hz^2 (Figure 2), which is the average σ_s^2 value from all the sources. Here, we use a subband of 0 ~ 120 Hz to calculate σ_s^2 to avoid errors from the noise. The *Q* value is estimated to be about 18, which is a typical value for near-surface sandy soil with significant absorption. The estimated *Q* value is used to correct the recorded data for attenuation, where Figures 3a and 3b show CSG #17 before and after the attenuation correction. A band-pass filter of 15 to 70 Hz is applied to the data set, and a 3D to 2D correction is also applied. Only the events that arrived within three to four periods after the first arrival are used. Figure 3c shows CSG #17 after all the processing steps. A natural source wavelet is extracted by averaging 10 to 20 near offset first arrivals aligned by cross-correlation in the space-time domain (Figure 4).

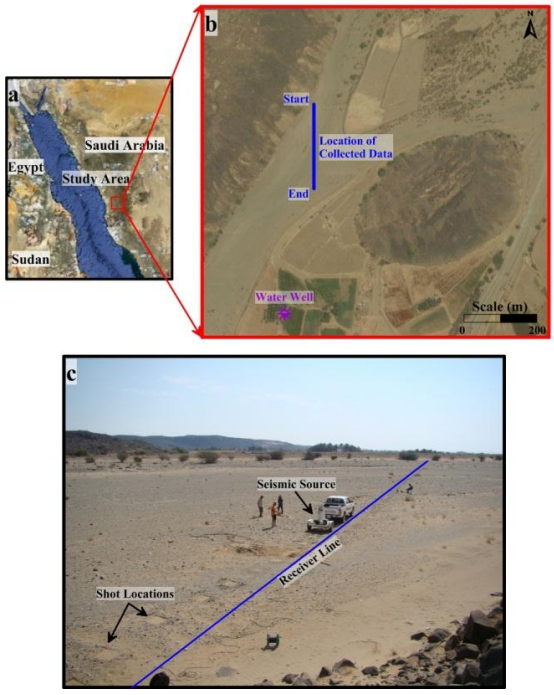

Figure 1: (a) Map of the study area at Wadi Qudaid, b). the blue line represents the location of the seismic profile, and the water well is denoted by the purple lettering. (c) A photo taken during data collection, blue line shows the locations of the receiver points.

DOI http://dx.doi.org/10.1190/segam2013-0351.1

Figures 5a and 5b show the traveltime and EWI tomograms after 30 iterations, respectively. The traveltime tomogram is used as the initial velocity model for the EWI inversion. Compared to the traveltime tomogram, EWI provides a highly resolved velocity model. The red line in Figures 5a and 5b represents the boundary between the first layer (Figure 6a) which consists of lose sand with gravels and the second layer (Figure 6b) which consists of compact sand with some gravel and partially to fully saturated with water. The black line represents the boundary between the second and the third layers which consists of highly fractured igneous rocks.

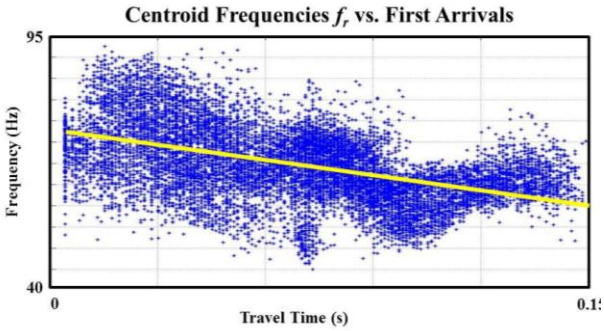

Figure 2: Pairs of f_r and the first arrival traveltimes t. The attenuation factor Q is estimated to be 18 by the best-fit line is denoted by the solid yellow line.

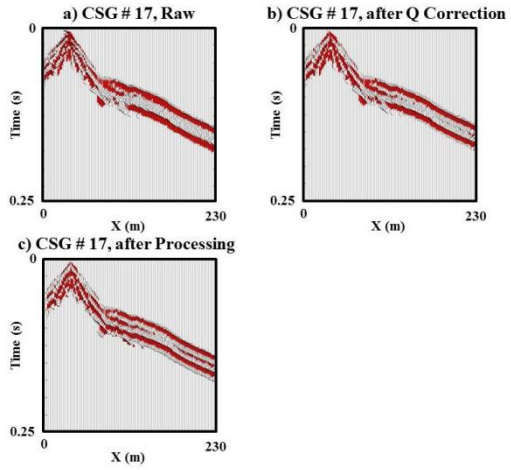

Figure 3: Early arrivals of (a) the original, (b) corrected for attenuation, and (c) the processed CSG #17.

Figure 7 compares the processed CSG #28 with the synthetic CSG #28 calculated from the EWI tomogram after 30 iterations. From Figure 7, many early arriving events in the synthetic data correlate well with the observed data. We estimate that there is around 18% more storage capacity for water in the EWI tomogram than in the traveltime tomogram. This extra capacity can make a significant difference when deciding to invest in transforming this wadi into an underground water reservoir. However, there is no ground truth that validates our estimate.

Figure 4: Source wavelet used in EWI. We extracted it from the recorded data by averaging 10 to 20 near offset first arrivals aligned by cross-correlation

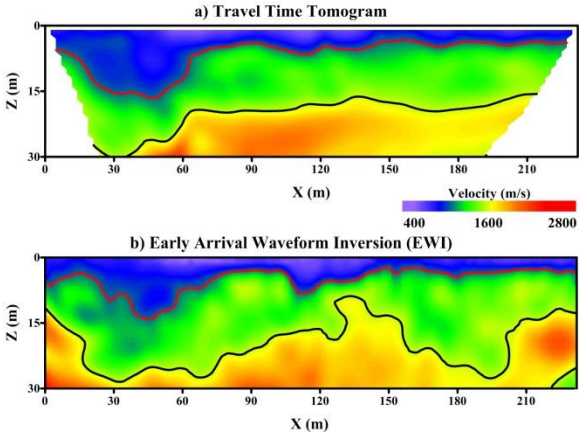

Figure 5: (a) The traveltime tomogram and (b) the EWI tomogram after 30 iterations. The red line represents the boundary between the surface layer and the compact sand layer, and the black line represents the boundary between the compact sand layer and the bedrock.

Figure 6: Two photos show soil from the (a) first layer and (b) the second layer at Wadi Qudaid. (b) is taken from inside the water well located southern of the site (Figure 1b).

DOI http://dx.doi.org/10.1190/segam2013-0351.1

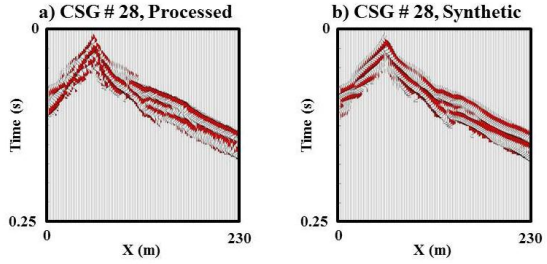

Figure 7: (a) Processed CSG #28, (b) synthetic CSG #28 based on the EWI tomogram.

Synthetic Test

We used the EWI tomogram to generate 117 CSGs using a finite-difference solution of the acoustic wave equation. The source and receiver geometries are identical to that used for the field data recorded at Wadi Qudaid. This data set is used to test the EWI approach described in this work. Figure 8a shows the true velocity model used to generate the synthetic CSGs, Figure 8b is a smoothed velocity model used as the initial velocity model for the EWI, and Figure 8c is the final tomogram after 30 iterations of EWI.

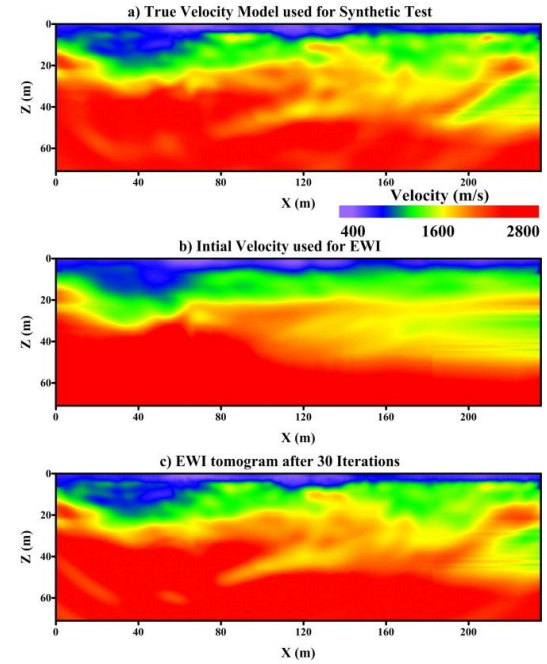

Figure 8: The result of the synthetic test; (a) the true velocity model used to generate the shot gathers, (b) the smoothed velocity model used as initial input to the early arrival wave form inversion (EWI), and (c) the EWI tomogram after 30 iterations.

The similarities between the true (Figure 8a) and the EWI (Figure 8c) velocity tomograms indicates that the EWI approach we use is suitable to process the shallow seismic data.

Conclusions

The early arrival waveform inversion (EWI) method is used to invert seismic data collected at Wadi Qudiad. EWI can be successfully applied to near-surface surveys if careful processing steps are carried out before inversion such as bandpass filtering, corrections for 3D geometric spreading, attenuation compensation, trace normalization, and source wavelet extraction. Our results show that EWI can provide a highly resolved subsurface velocity model compared to traveltime tomography. The drawbacks of EWI compared to traveltime tomography include complicated processing steps, higher computational cost, and slow convergence. Moreover, EWI fits complex waveforms instead of arrival times, which can be often characterized by getting stuck in a local minimum. Our future work includes using the multiscale method (Boonyasiriwat et al., 2010) to carry out EWI and gradually increasing the data window to image deeper structures. We also will use our towed land streamer system to efficiently collect shallow seismic data, and eventually invert these data in almost real time using the EWI approach. Compared to traveltime tomography, we believe that the more accurate EWI tomogram will make an economically important difference in assessing the storage potential of this wadi. It might also suggest the same for economic characterization of wadis throughout the world.

Acknowledgements

We would like to thank the 2012 sponsors of the CSIM Consortium (http://csim.kaust.edu.sa/web/) for their support. We thank the high performance computing (HPC) center of KAUST for providing the computational resources Shaheen (http://hpc.kaust.edu.sa/) for inversion. We thank Landmark for the University Software Grant and the permission to use ProMax.

DOI http://dx.doi.org/10.1190/segam2013-0351.1

http://dx.doi.org/10.1190/segam2013-0351.1

EDITED REFERENCES

Note: This reference list is a copy-edited version of the reference list submitted by the author. Reference lists for the 2013 SEG Technical Program Expanded Abstracts have been copy edited so that references provided with the online metadata for each paper will achieve a high degree of linking to cited sources that appear on the Web.

REFERENCES

Boonyasiriwat, C., G. T. Schuster, P. Valasek, and W. Cao, 2010, Applications of multiscale waveform inversion to marine data using a flooding technique and dynamic early-arrival windows: Geophysics, **75**, no. 6, R129–R136, http://dx.doi.org/10.1190/1.3507237.

Buddenseik, M., 2004, Colluvial wedge imaging using traveltime tomography along the Wasatch fault near Mapleton, Utah: M. S. thesis, University of Utah.

Causse, E., R. Mittet, and B. Ursin, 1999, Preconditioning for full-waveform inversion in viscoacoustic media: Geophysics, **64**, 130–145, http://dx.doi.org/10.1190/1.1444510.

Levander, A. R., 1988, Fourth-order finite-difference P-SV seismograms: Geophysics, **53**, 1425–1436, http://dx.doi.org/10.1190/1.1442422.

Liao, Q., and G. A. McMechan, 1997, Tomographic imaging of velocity and Q, with application to crosswell seismic data from the Gypsy Pilot site, Oklahoma: Geophysics, **62**, 1804–1811, http://dx.doi.org/10.1190/1.1444281.

Logan, J. D., 1996. Applied mathematics, 2nd edition: Wiley-Interscience.

Luo, Y., and G. T. Schuster, 1991, Wave equation traveltime inversion: Geophysics, **56**, 645–653, http://dx.doi.org/10.1190/1.1443081.

Nocedal, J., and S. J. Wright, 1999, Numerical optimization: Springer.

Pratt, G., C. Shin, and Hicks, 1998, Gauss-newton and full Newton methods in frequency space seismic waveform inversion: Geophysical Journal International, **133**, 341–362, http://dx.doi.org/10.1046/j.1365-246X.1998.00498.x.

Sheng, J., A. Leeds, M. Buddensiek, and G. T. Schuster, 2006, Early arrival waveform tomography on near-surface refraction data: Geophysics, **71**, no. 4, U47–U57, http://dx.doi.org/10.1190/1.2210969.

Tarantola, A., 1984, Inversion of seismic reflection data in the acoustic approximation: Geophysics, **49**, 1259–1266, http://dx.doi.org/10.1190/1.1441754.

Zhou, C., W. Cai, Y. Luo, G. T. Schuster, and S. Hassanzadeh, 1995, Acoustic wave-equation traveltime and waveform inversion of crosshole seismic data: Geophysics, **60**, 765–773, http://dx.doi.org/10.1190/1.1443815.